

Charm Production at RHIC

A. G. Knospe

Physics Department, Yale University, New Haven, CT 06520, USA

Observations by the PHENIX and STAR collaborations suggest that a strongly coupled quark-gluon plasma is produced in heavy-ion collisions at the Relativistic Heavy Ion Collider (RHIC). After a brief introduction to heavy-ion physics, measurements of heavy-quark production in heavy-ion collisions and the modification of heavy-quark spectra by the QGP are presented. Measurements of the total charm cross-section in several different collision systems confirm that $c\bar{c}$ pairs are produced through parton hard-scattering in the initial stages of the collisions. Non-photonic e^\pm (proxies for heavy quarks) are suppressed by a factor of ~ 5 in central Au + Au collisions relative to $p + p$ collisions. This is larger than most current theoretical predictions and has led to a re-examination of heavy-quark energy loss in the medium. The relative contributions of c and b decays to the non-photonic e^\pm spectrum have been predicted by perturbative QCD calculations; STAR measurements of azimuthal correlation functions of non-photonic e^\pm and hadrons agree with these predictions.

1. Introduction

The main purpose of the PHENIX and STAR experiments at the Relativistic Heavy Ion Collider is to study the properties of strongly interacting matter at high temperatures. Figure 1 shows a schematic theoretical phase diagram of nuclear matter for various temperatures and baryon chemical potentials [1, 2]. At normal baryon chemical potentials and low temperatures, strongly interacting matter exists as nuclei or a gas of interacting hadrons. At higher temperatures, however, the quarks may become deconfined due to asymptotic freedom; the degrees of freedom of the system are not hadrons, but individual quarks and gluons. This state of matter, called the quark-gluon plasma (QGP), is thought to have existed in the first few microseconds following the Big Bang, and may also have been produced in high-energy nucleus-nucleus collisions such as those at RHIC at Brookhaven National Laboratory and the SPS at CERN.

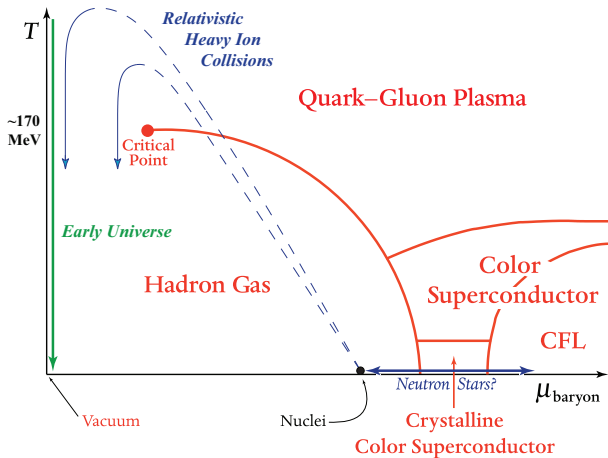


Figure 1: Schematic phase diagram of strongly interacting matter. On the vertical axis is temperature and on the horizontal axis is baryon chemical potential, μ_{baryon} .

Lattice QCD calculations predict a sudden increase in the number of degrees of freedom of strongly interacting matter near a critical temperature $T_C \sim 170$ MeV [1]. Whether or not there is a true phase transition and its exact nature has yet to be determined. It has been proposed that a critical point may exist in the phase diagram, and that for higher baryon densities, a first-order phase transition may be observed [1, 2]. A search for this critical point may be conducted in the next few years at RHIC by reducing the collision CM energy to lower values (~ 5 GeV) than the collider's present operating range (22 GeV to 200 GeV).

The collision of two nuclei introduces a large amount of energy into a region of space approximately the size of a nucleus for a short period of time. Lattice calculations predict a critical energy density of ≈ 700 MeV/fm³ needed for QGP formation [1]. The highest-energy RHIC collisions reach an energy density of at least 4.9 GeV/fm³, seven times the critical energy density [3]. The QCD vacuum is "melted" and a quark-gluon plasma is produced. It is believed that the QGP quickly reaches thermal equilibrium, expands, and cools for a few fm/c until the transition temperature is reached. At this point, the partons become confined into hadrons. The hadron gas expands and the hadrons scatter inelastically until chemical freeze-out. The hadron gas continues to expand for a few more fm/c with elastic hadron-hadron interactions until thermal freeze-out, after which hadronic interactions are negligible [4]. The resulting shower of particles can be detected in detector systems at RHIC.

Many phenomena in heavy-ion physics depend upon the degree of overlap between the two colliding nuclei, called the centrality of the collision. If the distance between the centers of the nuclei (impact parameter) is small, the overlap between the nuclei is large. Such collisions are called "central" events. A peripheral event has a small overlap and the impact parameter approaches the sum of the radii of the two nuclei. N_{part} is the number of nucleons that partici-

pate in collisions and N_{binary} is the number of binary collisions between those participating nucleons. N_{part} and N_{binary} are large for central events and small for peripheral events. The centrality of an event is estimated using the multiplicity of charged tracks at mid-rapidity. Central collisions are characterized by a higher charged-particle multiplicity than peripheral events. N_{part} and N_{binary} are estimated using the Glauber model of nucleus-nucleus interactions [5, 6].

The ratios of various particle yields have been fit with statistical thermal models, which indicate that at the time of chemical freeze-out, the system is thermalized and has a temperature $T = 170 - 180$ MeV for RHIC collision energies [7]. A non-central collision will have a spatially asymmetric overlap region, roughly elliptically shaped. The spatial asymmetry translates into a momentum-space asymmetry in the spectra of final state particles, with hadrons emitted preferentially near the reaction plane (the plane containing the beam axis and the impact parameter vector). Measurements of this phenomenon (called elliptic flow) are well described by ideal hydrodynamical models, indicating that the state of matter produced in the collision has a very low viscosity and is a nearly perfect liquid [8, 9, 10]. All RHIC experiments have observed the production of back-to-back di-jets in $p + p$, $d + \text{Au}$, and peripheral $\text{Au} + \text{Au}$ collisions. In central $\text{Au} + \text{Au}$ collisions, however, di-jets are not observed: the away-side jets appear to have been quenched by the medium [11, 12].

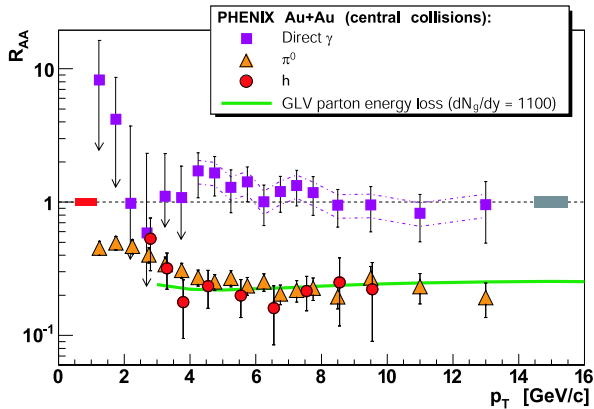


Figure 2: Nuclear Modification Factor, R_{AA} , for light-flavor hadrons and direct photons. π^0 and η are suppressed by a factor of ~ 5 in central $\text{Au} + \text{Au}$ collisions at $\sqrt{s_{NN}} = 200$ GeV relative to $p + p$ collisions at the same energy. Direct photons are not suppressed. The curve was generated using a theoretical model of parton interactions with the QGP. The data are used to constrain the value of the gluon density (dN_g/dy) in that model.

Hard-scattering processes (those with large momentum transfer) between the incoming nucleons are expected to account for 30-50% of the particles produced in a nucleus-nucleus collision. Hard scattering often produces particles with high transverse mo-

mentum ($p_T > 2$ GeV/c). Partons passing through a quark-gluon plasma are expected to lose energy to the medium through gluon radiation and collisions with other partons in the medium [13, 14]. The production of a QGP in a nucleus-nucleus collision will therefore cause a depletion of high- p_T particles relative to proton-proton collisions, which do not produce a medium. The standard measure of the effect of the medium on particle yields is the nuclear modification factor R_{AA} . R_{AA} is the ratio of a particle yield in nucleus-nucleus collisions to the yield produced in $p + p$ collisions. The ratio is scaled by $1/\langle N_{binary} \rangle$, where $\langle N_{binary} \rangle$ is the average number of nucleus-nucleon collisions in a nucleus-nucleus collision.

$$R_{AA} \equiv \frac{\frac{d^2 N(A+A)}{dp_T dy}}{\langle N_{binary} \rangle \frac{d^2 N(p+p)}{dp_T dy}} \quad (1)$$

If no medium is produced, then a nucleus-nucleus collision can be viewed as an incoherent superposition of nucleon-nucleon collisions and R_{AA} will be unity. Deviations from unity indicate the effects of nuclear matter and the quark-gluon plasma on particle yields. Central collisions produce a larger medium than peripheral collisions, which should result in a greater suppression of high- p_T particles.

Figure 2 shows measurements of R_{AA} for direct photons, π^0 , and η by PHENIX. R_{AA} is unity for direct photons [15], indicating that there is no suppression of direct photons in nucleus-nucleus collisions. This is expected since photons do not interact strongly and should not be affected by the presence of a QGP. However, the hadrons [16, 17, 18] are suppressed by about a factor of 5 at high p_T . Also shown is a theoretical prediction of light-flavor-hadron suppression from the GLV model of parton-QGP interactions [19, 20]. dN_g/dy is the gluon density, a parameter in the GLV model related to the opacity of the medium. The observed light-flavor-hadron suppression was used to constrain the value of this parameter, giving $dN_g/dy \approx 1100$. R_{AA} has also been measured for heavy-flavor decay products and compared to models; this will be discussed in subsequent sections. These and other measurements indicate that the matter produced in RHIC collisions is a strongly coupled quark-gluon plasma (sQGP) [21].

2. Experiments

The experiments described in these proceedings are conducted at the Relativistic Heavy Ion Collider (RHIC) at Brookhaven National Laboratory on Long Island, NY [22]. Ions are accelerated from the tandem Van de Graaff accelerators or the proton sources, through the AGS Booster and the AGS, and are injected into RHIC. Electrons are stripped off at several locations along the way. RHIC consists of two

synchrotron rings, 3.8 km in circumference. The two counter-circulating beams of ions intersect in each of the six interaction regions. The PHENIX and STAR detectors sit at two of these interaction regions. At RHIC, physicists can create and maintain beams of ions ranging from protons (both polarized and unpolarized) to the heaviest nuclei. RHIC can be used to collide protons with a center-of-mass collision energy up to $\sqrt{s} = 500$ GeV and a luminosity of $\sim 10^{32} \text{ cm}^{-2}\text{s}^{-1}$. RHIC can also collide ions ranging in mass from deuterons to gold nuclei with CM energy per nucleon pair $\sqrt{s_{NN}} \leq 200$ GeV and a luminosity of $\sim 10^{26} \text{ cm}^{-2}\text{s}^{-1}$ [23].

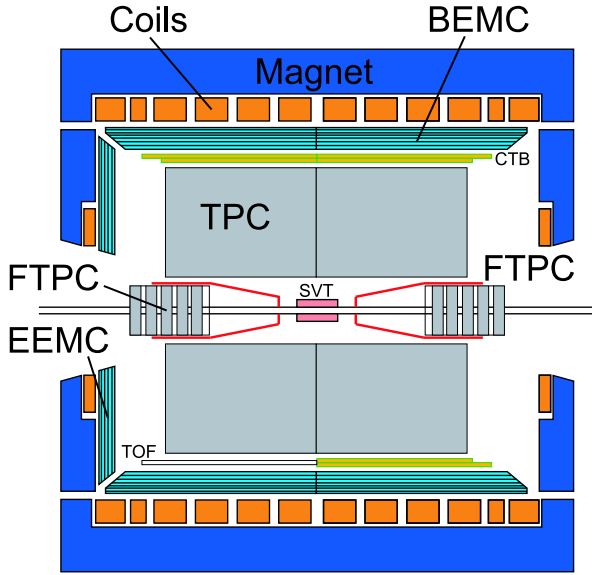


Figure 3: The STAR detector. Measurements described below use the Time Projection Chamber (TPC), Time-of-Flight detector (TOF), and the electromagnetic calorimeter (EMC).

Figure 3 shows a diagram of the STAR (Solenoidal Tracker At RHIC) detector [23]. The barrel and forward time-projection chambers (TPC and FTPC) record particle trajectories inside a room-temperature solenoidal 0.5-T magnet. The TPC covers pseudorapidity $|\eta| < 1.8$, while the FTPCs cover $2.5 < |\eta| < 4$. After passing through the TPC, particles enter the barrel electromagnetic calorimeter (BEMC) or the endcap electromagnetic calorimeter (EEMC, not shown). The STAR calorimeters together cover pseudorapidity $-1 < \eta < 2$. The Shower Maximum Detectors (SMDs), located approximately 5 radiation lengths inside each EMC tower module, provide additional particle identification based on the shape of the electromagnetic shower produced in the calorimeters. The SMDs allow shower shapes to be measured to high precision ($\Delta\eta = 0.007$, $\Delta\phi = 0.007$ rad). A silicon vertex tracker (SVT) covers $|\eta| < 1$ between the beampipe and the TPC, providing accurate particle tracking near the collision vertex. A prototype

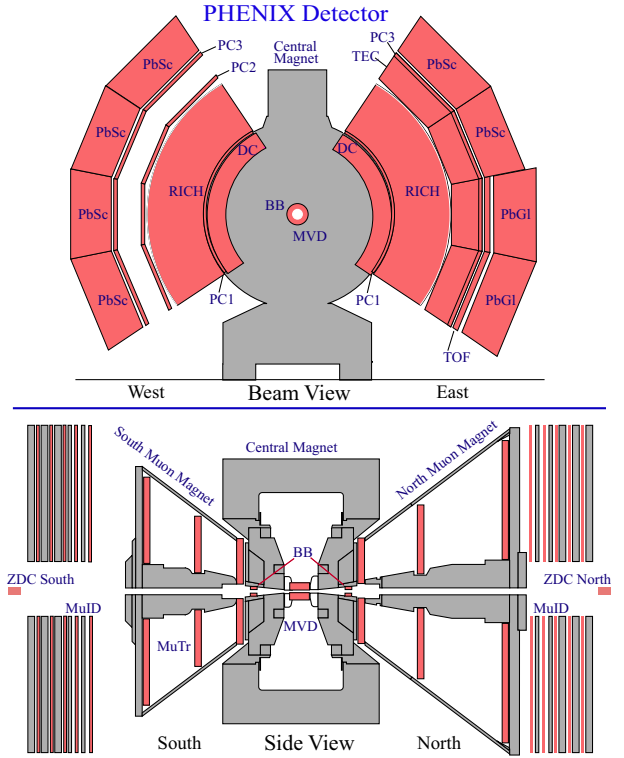


Figure 4: The PHENIX detector in 2003. Measurements described below use the Pad Chambers (PC), Drift Chambers (DC), Time Expansion Chambers (TEC), Ring-Imaging Cherenkov detectors (RICH), Time-of-Flight detector (TOF), and the lead-scintillator (PbSc) and lead-glass (PbGl) electromagnetic calorimeters.

Time-of-Flight detector (TOF) has been installed outside the TPC covering $-1 < \eta < 0$ and $\Delta\phi = 0.04$ rad. The TOF provides a precise measurement of particle velocity. Plans call for the TOF to be extended to full azimuthal coverage over pseudorapidity $|\eta| < 1$. A full description of the STAR detector is given in [23].

Figure 4 shows a diagram of the PHENIX (Pioneering High-Energy Nuclear Interaction Experiment) detector. [24] The two central spectrometer arms sit in an axial magnetic field and cover $|\eta| < 0.35$ and $\pi/2$ each in azimuth. Particle tracking is provided by three sets of pad chambers and (in the east arm) the time expansion chamber. The Ring-Imaging Cherenkov detectors and the Time-of-Flight detector provide particle identification. Beyond these detector systems sit lead-glass and lead-scintillator calorimeters. The two forward muon spectrometer arms sit in radial magnetic fields. They consist of drift chambers for precision tracking and muon identifiers. The muon identifiers are made up of alternating layers of steel absorber plates and streamer-tube tracking layers. A full description of the PHENIX detector, including the azimuthal and pseudorapidity coverage of each detector subsystem, is given in [24].

3. Heavy Flavors

Due to the high luminosity at RHIC, even particles with comparatively low production cross-sections, such as c and b quarks, can be used to probe the strongly interacting matter produced. In nucleus-nucleus collisions, the dominant production mechanism for heavy quarks is gluon-gluon fusion in the initial hard scattering of nucleons [25]. Thermal production of heavy-quark pairs in the medium is believed to be negligible after the initial stages of the collision and the number of heavy quarks is essentially "frozen." Therefore, heavy quarks are probes sensitive to all stages in the evolution of the QGP, from its initial formation to hadronization and freeze-out.

The presence of a QGP is expected to lead to the dissociation and suppression of heavy quarkonia through Debye screening of color charges. Some theoretical calculations predict sequential dissociation of heavy quarkonia, with the more weakly bound resonances dissociating at lower temperatures [26]. If this is true, measurements of heavy quarkonium suppression could lead to a measurement of the initial temperature of the medium. PHENIX measurements of R_{AA} for J/ψ [27, 28, 29] show less suppression than was expected based on SPS data. This may be due to the regeneration of J/ψ through the recombination of dissociated charm (anti)quarks into new $c\bar{c}$ pairs [30, 31, 32, 33, 34].

While all partons lose energy to the medium through gluon bremsstrahlung, the intensity and angular distribution of the gluon radiation is predicted to depend upon the mass of the radiating parton. In the small-angle approximation, the angular distribution of gluon radiation from heavy quarks differs from the bremsstrahlung spectrum for massless partons by the pre-factor given in equation 2.

$$\frac{dP(\text{heavy quark})}{d\theta^2} = \left(1 + \frac{M_Q}{E_Q} \cdot \frac{1}{\theta^2}\right)^{-2} \frac{dP(\text{light quark})}{d\theta^2} \quad (2)$$

where M_Q and E_Q are the heavy-quark mass and energy, respectively [35]. This suppression of gluon radiation from heavy quarks is strongest for angles less than M_Q/E_Q . The suppression of small-angle gluon radiation is called the dead cone effect. Because of the dead cone effect, heavy quarks should lose less energy to the medium through gluon radiation than light quarks. Partons can also lose energy through collisions with other partons in the medium. For heavy quarks traversing the medium, the amount of energy lost through collisions may be comparable to the amount lost through gluon radiation [13, 14].

4. Measurements of Open Heavy Flavors

The RHIC experiments have studied several different heavy-flavor decay channels, including the hadronic decays of D^0 mesons to pions and kaons, and the semileptonic decays of heavy-flavor hadrons to muons and electrons.

4.1. Direct Reconstruction of D^0 Decays

The STAR collaboration has found the yields of D^0 and \bar{D}^0 mesons [36] by reconstructing the $D^0(\bar{D}^0) \rightarrow K^\mp + \pi^\pm$ decays, which have a branching ratio of 3.83% [37]. The pions and kaons are identified by their energy loss in the Time Projection Chamber. STAR cannot reconstruct the full decay topology since $c\tau(D^0) = 124 \mu\text{m}$ [37] and the TPC does not have sufficient track projection resolution to distinguish D^0 decay products from tracks coming directly from the primary collision vertex. The D^0 invariant mass spectrum was obtained by pairing each kaon with oppositely charged pions from the same event. The combinatorial background was estimated through event mixing techniques and subtracted. Figure 5a shows the $K\pi$ invariant mass spectrum for $|y| < 1$ in Au + Au collisions at $\sqrt{s_{NN}} = 200 \text{ GeV}$ [38]. A clear D^0 peak is visible. Because of the small branching ratio for this decay and the lack of a dedicated trigger, this analysis is limited by statistics to $p_T < 3 \text{ GeV}/c$.

4.2. Decays to Muons

The STAR collaboration has identified low- p_T muons ($0.17 \text{ GeV}/c < p_T < 0.25 \text{ GeV}/c$) through measurements of energy loss in the Time Projection Chamber and $m^2 = (p/(\beta\gamma))^2$ in the Time-of-Flight detector and the TPC. Figure 5b shows the m^2 distribution of particles after energy-loss selection [39]. The muon and pion peaks are clearly visible. In addition to muons from heavy flavor decays, the muon peak contains a large number of muons from pion and kaon decays; it was necessary to remove these "background" muons. HIJING [40] was used to simulate the DCA (distance of closest approach) of muon tracks with the primary collision vertex (see Figure 5c). The DCA distribution for muons from charm decays has a maximum much closer to zero than the distribution for muons from pion and kaon decays. The observed DCA distribution was fit with a linear combination of these two simulated DCA distributions to obtain the contribution of charm-decay muons to the total muon yield. [39]

4.3. Decays to Single Electrons

Both the PHENIX and STAR collaborations have also studied the spectrum of single electrons, i.e. e^\pm

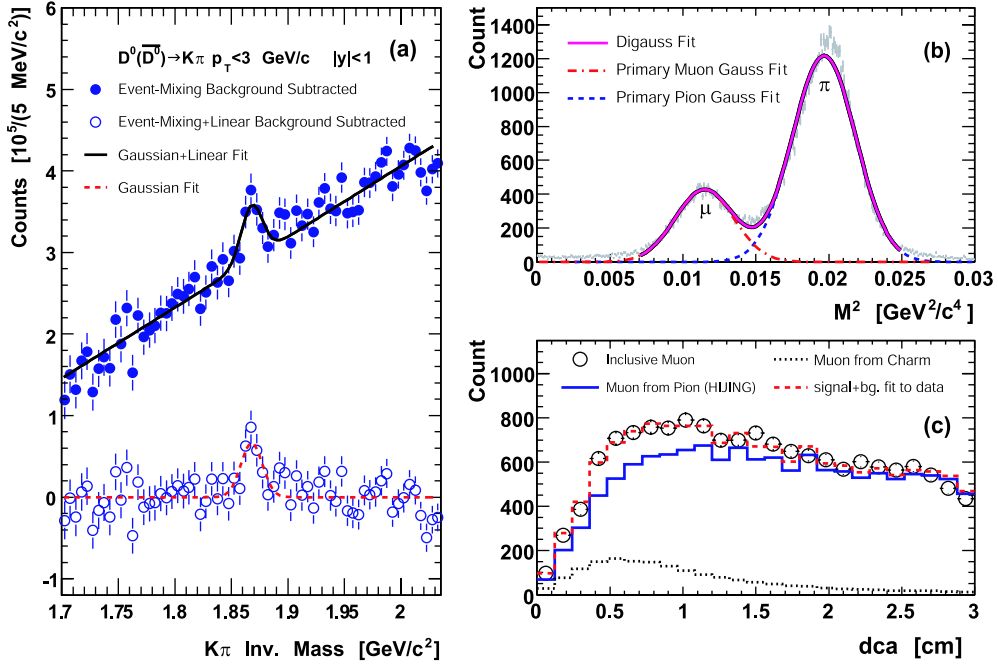


Figure 5: STAR heavy-flavor identification methods. (a) D^0 meson reconstruction in 200-GeV Au+Au collisions. The $K\pi$ invariant mass distribution is shown after the subtraction of the combinatorial background (estimated using event-mixing). The residual background is approximated by a linear function and subtracted. (b) m^2 distribution measured by TOF detector in 200-GeV Au + Au collisions. The particles have passed the energy-loss cut used to identify low- p_T muons. (c) DCA distributions used to identify charm-decay contribution to the inclusive muon spectrum (see explanation in text).

produced with (anti)neutrinos in weak decays. The spectrum of single e^\pm is expected to be dominated by heavy-flavor semileptonic decays (e.g. $D^0 \rightarrow e^+ + K^- + \nu_e$). The main sources of background to the single e^\pm signal are e^+e^- pairs from π^0 and η Dalitz decays and photon conversions [37]. For this reason, single e^\pm are called non-photonic e^\pm , while the background e^\pm are called photonic e^\pm . The decays of vector mesons (e.g. ρ , ϕ , and ω) make small contributions to the photonic e^\pm background. Background e^\pm from photon conversion is less significant at PHENIX due to the reduced amount of material relative to STAR. K_{e3} decays ($K^\pm \rightarrow \pi^0 + e^\pm + \nu_e(\bar{\nu}_e)$) and $K_L^0 \rightarrow \pi^\mp + e^\pm + \nu_e(\bar{\nu}_e)$ make small contributions to the single e^\pm signal.

The STAR collaboration identifies e^\pm using two different methods. For $p_T < 3.5$ GeV/c, e^\pm are identified through measurements of energy loss and m^2 with the Time Projection Chamber and Time-of-Flight detector (similar to the method of muon identification described above) [36]. For $p_T > 1.5$ GeV/c, e^\pm are identified through measurements of TPC energy loss, the energy E deposited in the electromagnetic calorimeter, and the shape of the electromagnetic shower measured in the shower maximum detector [41]. The use of a trigger allows this measurement to extend up to $p_T \approx 8$ GeV/c. An energy-loss cut of approximately $3.5 \text{ keV/cm} < dE/dx < 5 \text{ keV/cm}$ is used to identify

e^\pm (the exact bounds are varied slightly depending on track momentum and event charged-track multiplicity). Compared to hadrons, e^\pm produce larger showers and deposit more of their energy in the EMC. The ratio p/E has a maximum near 1 for e^\pm (see Figure 6 [42]) and additional e^\pm identification is provided by cuts on the shower size in the SMD. The remaining hadron contamination is $\approx 2\%$ at $p_T \sim 2$ GeV/c and $\approx 20\%$ at $p_T \sim 8$ GeV/c. STAR identifies photonic (background) e^\pm through invariant-mass reconstruction of e^+e^- pairs. The invariant-mass distribution of e^+e^- pairs from photon conversions and π^0 and η Dalitz decays has a maximum near 0 mass. When a cut of $M_{inv}(e^+e^-) < 150 \text{ MeV}/c^2$ is used, photonic electrons are identified with an efficiency around 70%.

The PHENIX collaboration identifies e^\pm using the Ring-Imaging Cherenkov detector, measurements of the shower shape in the electromagnetic calorimeter, and a cut on the energy-to-momentum ratio [43, 44]. Photonic e^\pm are identified using two different methods. In the "cocktail subtraction" method, the spectra of e^\pm from various sources of background are simulated. Measured yields of π^0 , η , direct photons, and other sources of background are used as input for the simulation generator. In the "converter subtraction" method, a photon converter (a thin brass sheet of $1.67\% X_0$) is inserted around the beam pipe. ΔN_e , the increase in the e^\pm yield due to the converter, is

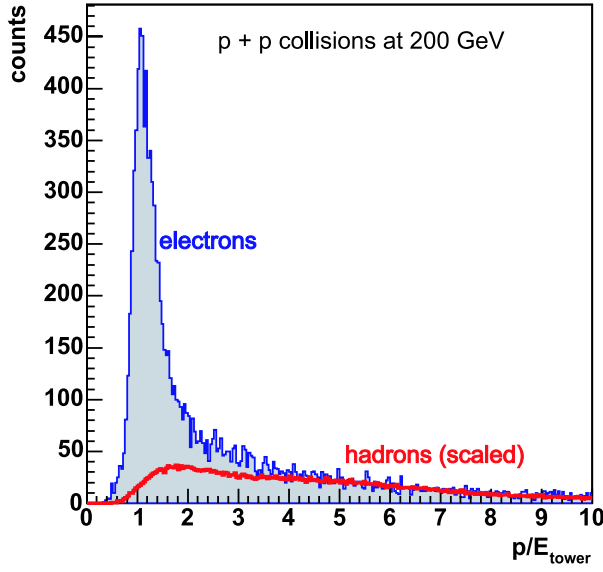


Figure 6: p/E distributions for e^\pm and hadrons in 200-GeV $p+p$ collisions at STAR. e^\pm and hadrons are identified through their energy loss in the Time Projection Chamber. The hadron distribution has been scaled to match the e^\pm distribution at high values of p/E . This provides an estimate of the hadron background that remains in the e^\pm peak.

measured. GEANT simulations are used to determine R_γ , the fractional increase in the photonic e^\pm yield caused by the converter ($R_\gamma \approx 2.3$ in the 2006 $p+p$ run). Knowledge of ΔN_e and R_γ allows the photonic e^\pm yield to be determined and removed from the inclusive e^\pm yield. Where $N_{\gamma e}^{NC}$ is the photonic e^\pm yield with no converter present,

$$N_{\gamma e}^{NC} = \frac{\Delta N_e}{R_\gamma - 1}. \quad (3)$$

The non-photonic e^\pm yields measured using the cocktail and converter subtraction methods are consistent with each other.

5. Total Charm Cross-Section

STAR determines the total charm cross-section, $\sigma_{c\bar{c}}$, for each collision system through a combined fit of the D^0 , muon, and non-photonic e^\pm measurements described above (e.g. Figure 7a for 200-GeV Au + Au collisions) [39]. PHENIX determines the total charm cross-section from the measurement of the non-photonic e^\pm yield (e.g. Figure 7b for 200-GeV $p+p$ collisions) [43]. Figure 8a shows measurements of the scaled total charm cross-section by STAR and PHENIX for $p+p$ [43], $d+Au$ [36], and Au + Au [41, 44] collisions (in different centrality bins) at $\sqrt{s_{NN}} = 200$ GeV. A preliminary STAR measurement for Cu + Cu using only D^0 reconstruction is also

shown [45]. The cross-section is divided by $\langle N_{binary} \rangle$, the average number of binary collisions for the given collision system. Within each experiment, the charm cross-section scales with the number of binary collisions. This is a confirmation that charm is indeed produced through initial parton hard-scattering and that charm production through other mechanisms (such as thermal production in the QGP) is not significant. Note that the cross-sections measured by STAR are higher than those measured by PHENIX by a factor of ~ 2 . This is still under investigation.

Due to the large quark masses, the hard-scattering processes that produce heavy flavor can be calculated using perturbative QCD [46]. The most advanced perturbative calculation scheme is the Fixed-Order plus Next-to-Leading-Log-resummed approximation, or FONLL. A FONLL prediction for the charm cross-section [47, 48] is shown as prediction (I) in Figure 8a. The PHENIX data are consistent with this prediction; the STAR data are greater than the FONLL prediction by a factor of ~ 5 and sit well above the upper uncertainty bound. However, the charm cross-section predictions are sensitive to the number of active flavors, the choice of scale, and the parton densities in the collision system. A new calculation by R. Vogt [48] (prediction (II) in Figure 8a) indicates that the uncertainties on the perturbative calculation may be larger than previously thought. The total charm cross-section measured by STAR is consistent with the new perturbative calculation.

Figure 8b shows the ratios of the measured non-photonic e^\pm yields [36, 41, 43] to the FONLL prediction as functions of p_T for $p+p$ collisions at $\sqrt{s} = 200$ GeV. The dashed horizontal lines indicate the ratio of the measured cross-sections to the FONLL cross-section. Figure 8b indicates that STAR's disagreement with PHENIX (by a factor of ~ 2) and FONLL (by a factor of ~ 5) exists even at high p_T . However, the FONLL prediction does describe the shape of the STAR and PHENIX non-photonic e^\pm spectra well.

6. Medium Modification of Non-photonic e^\pm Spectra

The cross-section discrepancy between PHENIX and STAR cancels in the nuclear modification factor R_{AA} , which is the scaled ratio of particle yields (see definition above). Figure 9a shows R_{AA} of non-photonic e^\pm for Au + Au collisions at $\sqrt{s_{NN}} = 200$ GeV for both PHENIX [44] and STAR [41, 49]. R_{AA} is plotted as a function of $\langle N_{part} \rangle$, the average number of nucleons participating in collisions in a given centrality bin. The most central collisions have the highest values of $\langle N_{part} \rangle$. The PHENIX and STAR R_{AA} are consistent with each other across the range of $\langle N_{part} \rangle$ shown. Plotted in shaded bands are the values of R_{AA} measured by PHENIX for π^0 [16] and by

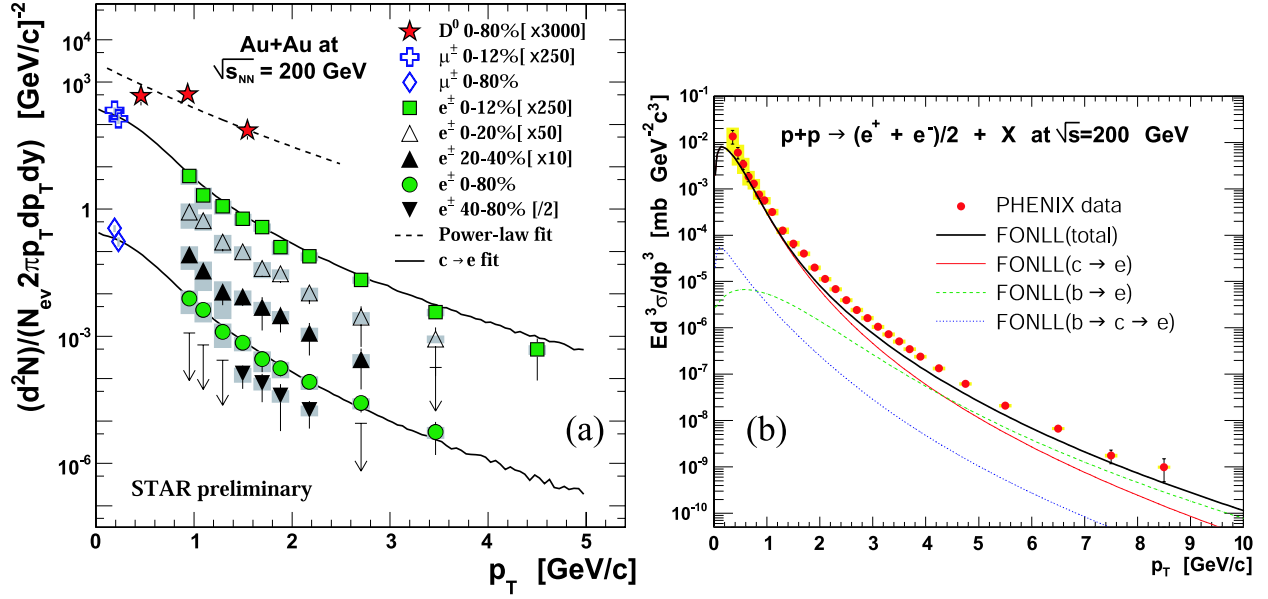


Figure 7: Measurements used in calculation of total charm cross-section. (a) STAR D^0 , muon, and e^\pm spectra for 200-GeV Au + Au collisions in various centrality bins. (b) PHENIX non-photonic e^\pm spectrum for 200-GeV $p + p$ collisions. Also shown are pQCD predictions (FONLL) for the c - and b -decay contributions to the spectrum (see discussion below and Figure 10).

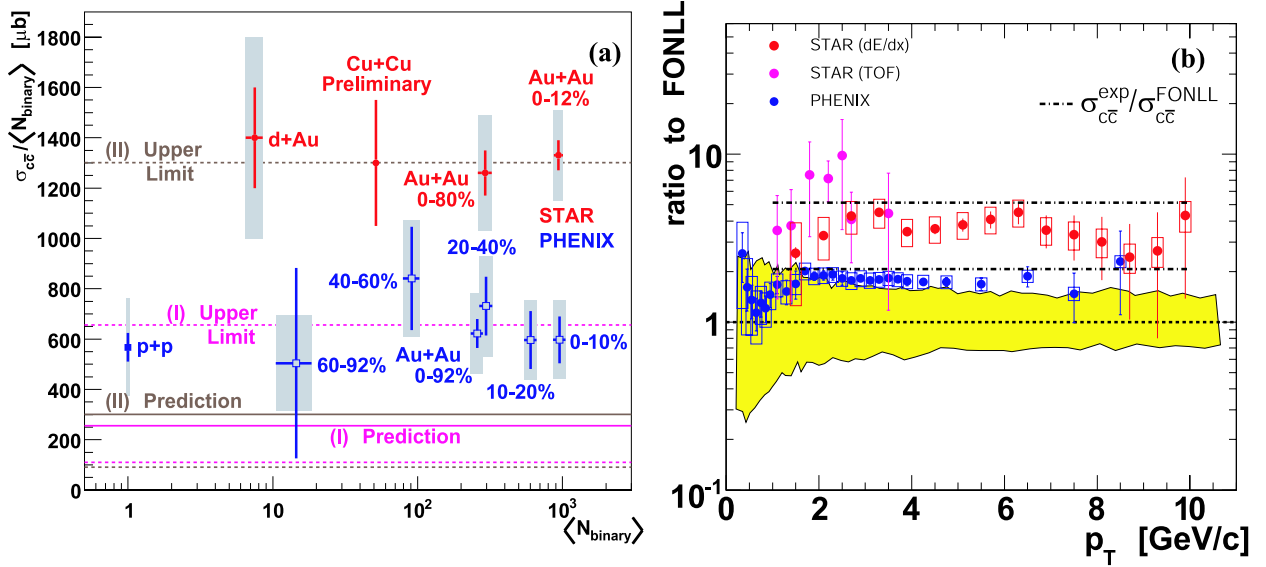


Figure 8: Comparisons of RHIC measurements to FONLL predictions. (a) Total charm cross-section (scaled by $1/\langle N_{baryon} \rangle$) in different collision systems at $\sqrt{s_{NN}} = 200$ GeV. Theoretical predictions are also shown. (b) Ratios of non-photonic e^\pm yields in central 200-GeV Au + Au collisions for STAR and PHENIX to FONLL prediction (I) in central 200-GeV Au + Au collisions. STAR e^\pm have been selected using measurements of energy-loss (dE/dx) in the TPC or m^2 in the TOF.

STAR for charged light-flavor hadrons [50]. The measured suppression of non-photonic e^\pm is similar to the suppression observed for light-flavor hadrons. This was unexpected, as heavy quarks were expected to lose less energy in the medium than light quarks. As a result, non-photonic e^\pm (proxies for heavy quarks) would be suppressed less than light-flavor hadrons.

Figure 9b shows a comparison of the non-photonic e^\pm suppression measured by STAR and PHENIX to several theoretical models of heavy-quark interactions with a quark-gluon plasma. The data are from central Au + Au collisions at $\sqrt{s_{NN}} = 200$ GeV. In $d + Au$ collisions at this energy a $\sim 50\%$ enhancement of non-photonic e^\pm is observed (data [41]) not

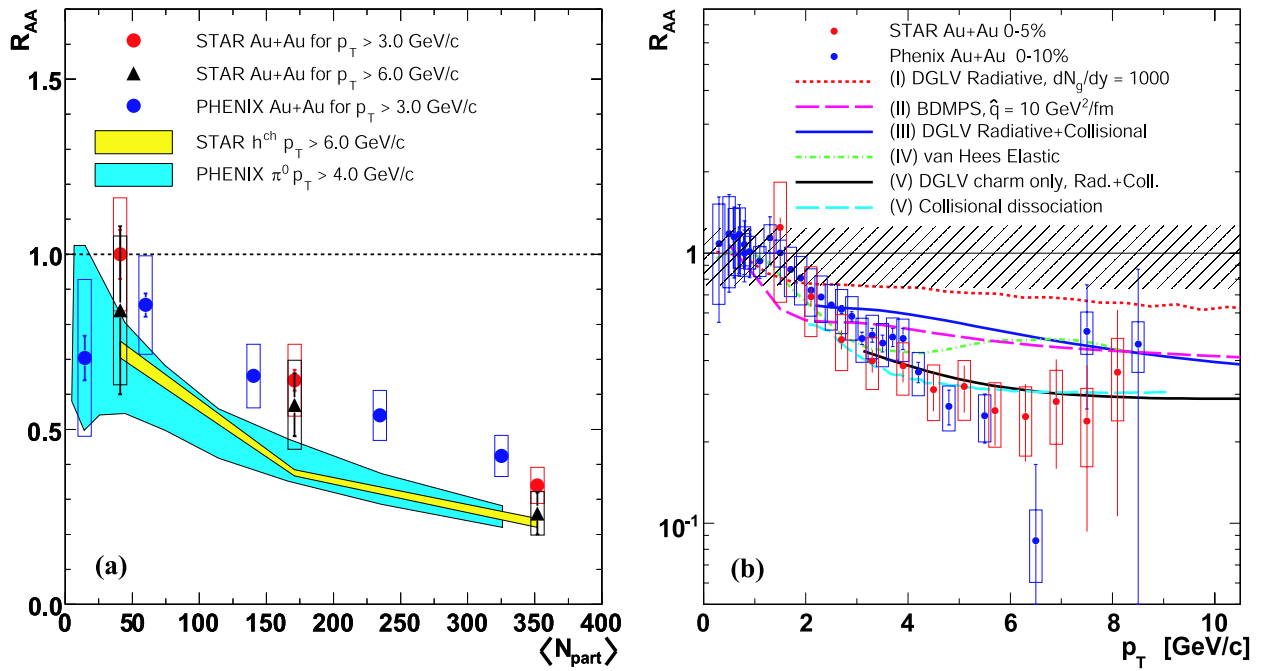


Figure 9: Nuclear modification factor (R_{AA}) for non-photonic e^\pm in Au + Au collisions at 200 GeV. (a) R_{AA} vs. $\langle N_{part} \rangle$. Also shown are light-flavor hadron R_{AA} data. (b) R_{AA} vs. p_T for central collisions. The data are compared to theoretical predictions.

shown). The enhancement is explained by the Cronin effect (multiple scattering in normal nuclear matter). Therefore, the strong non-phonic- e^\pm suppression observed in central Au + Au collisions does not appear to be due to such cold nuclear matter effects. The calculations that produce curves (I) and (II) include only energy loss through gluon radiation; these calculations under-predict the suppression of non-photonic e^\pm [51, 52]. dN_g/dy is the gluon density in the DGLV model (curve (I)) and \hat{q} is the time-averaged transport coefficient in the BDMPS model (curve (II)). These parameters are related to the opacity of the QGP, with higher values corresponding to a more opaque medium. Light-hadron suppression data are used to constrain the values of these parameters. The DGLV model with $dN_g/dy \approx 1000$ and the BDMPS model with $\hat{q} \approx 10 \text{ GeV}^2/\text{fm}$ describe the observed light-hadron suppression well.

In addition to energy loss through gluon radiation, partons can lose energy through collisions with other partons in the medium. Calculations [13] indicate that, for heavy quarks, collisional energy loss is as important as radiative energy loss. Curve (III) is generated using the DGLV model (which produced curve (I)) including both radiative and collisional energy loss [53]. Curve (IV) is generated using the model of van Hees *et al.* [54], which includes heavy-quark energy loss through elastic collisions in the medium and the formation of resonant D - and B -meson states through quark coalescence. Curves (III) and (IV) seem to describe the data better than curves (I) and

(II), which include only radiative energy loss, but still tend to under-predict the observed suppression of non-photonic e^\pm , especially at high p_T . The model of Adil and Vitev [55] (curve (VI)) uses the fragmentation of heavy quarks and the subsequent dissociation of D - and B -meson states in the medium to explain the suppression pattern of non-photonic e^\pm . This model does describe the observed suppression well.

Curves (I)-(IV) and (VI) were generated using FONLL predictions [47] for the relative contributions of c - and b -quark decays to the non-photonic e^\pm spectrum. Curve (V) is generated with the assumption that only c -quark decays contribute to the non-photonic e^\pm spectrum and that the b -quark contribution is insignificant for the p_T range shown [53]. Curve (V) (which includes both radiative and collisional energy loss) is consistent with the measured suppression. It is therefore important to disentangle the c and b contributions and determine their relative strengths; this will be discussed in the next section.

7. Electron-Hadron Azimuthal Correlations

Figure 10 shows FONLL calculations of the D - and D -meson-decay contributions to the non-photonic electron cross-section as functions of p_T [47]. The upper and lower limits result from the variation of model parameters including quark masses and renormaliza-

tion scales. The charm contribution is dominant at low p_T . The bottom contribution becomes larger than the charm contribution around $p_T \sim 5$ GeV/ c .

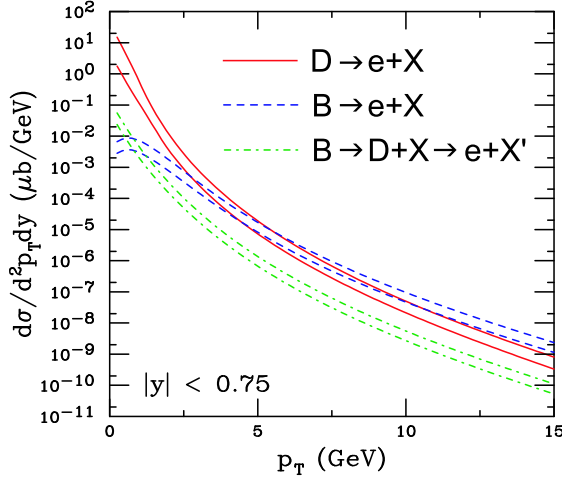


Figure 10: FONLL predictions for the contributions of D - and B -meson decays to the mid-rapidity non-photonic e^\pm cross-section at $\sqrt{s} = 200$ GeV.

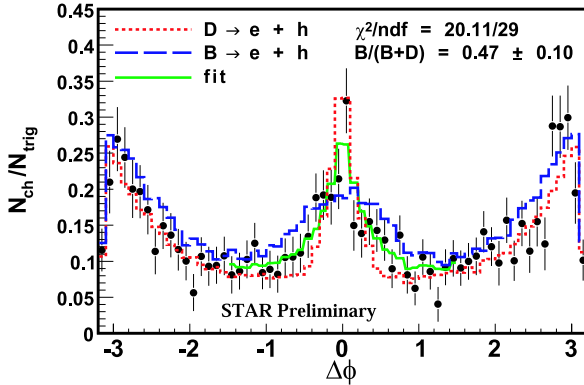


Figure 11: $\Delta\phi$ for pairs of non-photonic e^\pm and hadrons. $5.5 \text{ GeV}/c < p_T(e^\pm) < 6.5 \text{ GeV}/c$ and $p_T(h) > 0.3 \text{ GeV}/c$. On the vertical axis is the number of charged tracks per trigger e^\pm .

To disentangle the charm and bottom contributions, the STAR collaboration has studied azimuthal correlations between non-photonic e^\pm and hadrons. Figure 11 shows the difference in azimuthal angle ($\Delta\phi$) between non-photonic e^\pm and hadrons in 200-GeV proton-proton collisions for one p_T bin [56]. Due to decay kinematics, there will be an azimuthal correlation between the leptons and hadrons produced in heavy-flavor semi-leptonic decays. Due to the larger B -meson mass, a B -meson can give more kinetic energy to its decay products than a D -meson, resulting in a broader near-side ($\Delta\phi \sim 0$) correlation peak. The expected charm and bottom contributions to this distribution are simulated with PYTHIA. Varying the

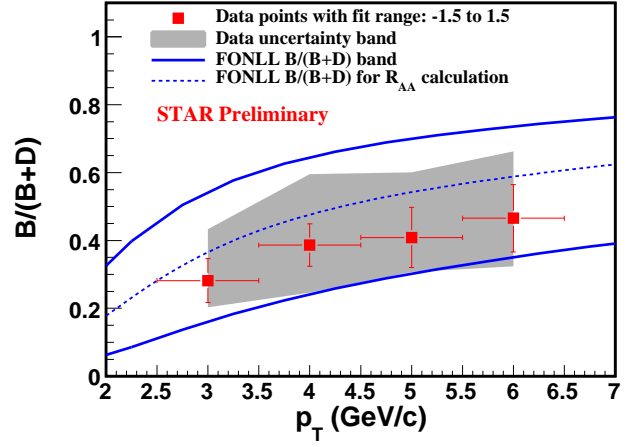


Figure 12: Fractional contribution of B -meson decays to the non-photonic e^\pm spectrum at $\sqrt{s} = 200$ GeV.

quark fragmentation functions inside PYTHIA does not significantly alter the shapes of the simulated $\Delta\phi$ distributions. The measured distribution is then fit with a linear combination of the simulated charm and bottom distributions to find their relative strengths. $B/(B+D)$, the fraction of the total non-photonic e^\pm cross-section due to B -meson decays, is plotted in Figure 12. The measurement of $B/(B+D)$ through e - h correlations [56] is consistent with FONLL predictions. This is an indication that b -quark suppression *should* be taken into account in describing the suppression of non-photonic e^\pm at moderate p_T (see the discussion in the previous section).

8. Conclusions

Measurements of jet quenching and elliptic flow suggest that the state of matter created in a heavy-ion collision at RHIC energies is a strongly coupled quark-gluon plasma (sQGP) [21] and is a near-perfect liquid [10]. PHENIX and STAR have calculated the total charm cross-section $\sigma_{c\bar{c}}$ for $p + p$, $d + \text{Au}$, $\text{Cu} + \text{Cu}$, and $\text{Au} + \text{Au}$ collisions at $\sqrt{s_{NN}} = 200$ GeV [36, 41, 43, 44, 45]. The cross-section scales with the number of binary nucleon-nucleon collisions, an indication that charm quarks are indeed produced through initial parton hard-scattering. PHENIX and STAR have measured the nuclear modification factor R_{AA} for light-flavor hadrons [18] and for non-photonic e^\pm , which come predominantly from heavy-flavor semileptonic decays [41, 43, 44]. The suppression of non-photonic e^\pm in central $\text{Au} + \text{Au}$ collisions is greater than expected. It has been difficult for theoretical models [51, 52, 53, 54, 55] to describe the suppression of light-flavor hadrons and non-photonic e^\pm simultaneously. Perturbative QCD calculations (FONLL) [47] predict that the b -decay contribution to the non-photonic e^\pm becomes comparable to the

c -decay contribution at $p_T \sim 5$ GeV/ c . STAR measures the difference in azimuth angle ϕ for pairs of non-photonic e^\pm and hadrons [56]. This distribution is fit with PYTHIA simulations of the expected c - and b -decay contributions to determine their relative strengths; these data are consistent with the FONLL predictions.

Acknowledgments

Thanks to J. W. Harris, J. Bielcik, H. Caines, and T. Ullrich for all they have taught. Thanks to the Heavy Flavor Working Group at STAR for their advice in preparing the talk. S. Salur and S. Baumgart provided valuable help in the preparation of this paper.

References

- [1] F. Karsch, *Nucl. Phys. A* **698** (2002) 199c
- [2] K. Kanaya, *Nucl. Phys. A* **715** (2003) 233c
- [3] J. Adams *et al.* (STAR Collaboration), *Phys. Rev. C* **70** (2004) 054907
- [4] J.-P. Blaizot, *Nucl. Phys. A* **661** (1999) 3c
- [5] R. J. Glauber, *Lectures on Theoretical Physics, Vol. 1*, p. 315 (1959)
- [6] J. Adams *et al.* (STAR Collaboration), *Phys. Rev. C* **70** (2004) 054907
- [7] P. Braun-Munzinger *et al.*, *Phys. Lett. B* **518** (2001) 41
- [8] C. Adler *et al.* (STAR Collaboration), *Phys. Rev. Lett.* **90** (2003) 032301
- [9] C. Adler *et al.* (STAR Collaboration), *Phys. Rev. Lett.* **87** (2001) 182301
- [10] C. Adler *et al.* (STAR Collaboration), *Phys. Rev. Lett.* **89** (2002) 132301
- [11] C. Adler *et al.* (STAR Collaboration), *Phys. Rev. Lett.* **90** (2003) 032301
- [12] C. Adler *et al.* (STAR Collaboration), *Phys. Rev. Lett.* **89** (2002) 202301
- [13] M. G. Mustafa, *Phys. Rev. C* **72** (2005) 014905
- [14] M. Djordjevic, *Phys. Rev. C* **74** (2006) 064907
- [15] S. S. Adler *et al.* (PHENIX Collaboration), *Phys. Rev. Lett.* **94** (2005) 232301
- [16] S. S. Adler *et al.* (PHENIX Collaboration), *Phys. Rev. Lett.* **91** (2003) 072301
- [17] S. S. Adler *et al.* (PHENIX Collaboration), *Phys. Rev. C* submitted, arXiv:nucl-ex/0611007v1 (2006)
- [18] S. S. Adler *et al.* (PHENIX Collaboration), *Phys. Rev. C* **75** (2007) 024909
- [19] I. Vitev and M. Gyulassy, *Phys. Rev. Lett.* **89** (2002) 252301
- [20] I. Vitev, *J. Phys. G* **30** (2004) S791
- [21] M. Gyulassy and L. McLerran, *Nucl. Phys. A* **750** (2005) 30-63
- [22] H. Hahn *et al.*, *Nucl. Instr. and Meth. A* **499** (2003) 245
- [23] K. H. Ackerman *et al.* (STAR Collaboration), *Nucl. Instr. and Meth. A* **499** (2003) 624-632
- [24] K. Adcox *et al.* (PHENIX Collaboration), *Nucl. Instr. and Meth. A* **499** (2003) 469
- [25] Z. Lin and M. Gyulassy, *Phys. Rev. C* **51** (1995) 2177
- [26] T. Matsui and H. Satz, *Phys. Lett. B* **178** (1986) 416
- [27] A. Adare, *et al.* (PHENIX Collaboration), arXiv:nucl-ex/0611020v1 (2006)
- [28] S. S. Adler *et al.* (PHENIX Collaboration), *Phys. Rev. Lett.* **96** (2006) 012304
- [29] R. Averbeck, *J. Phys. G* **34** (2007) S567-S574
- [30] P. Braun-Munzinger and J. Stachel, *Phys. Lett. B* **490** (2000) 196
- [31] P. Braun-Munzinger and J. Stachel, *Nucl. Phys. A* **690** (2001) 619c
- [32] L. Grandchamp *et al.*, *Phys. Rev. Lett.* **92** (2004) 212301
- [33] R. L. Thews and M. L. Mangano, *Phys. Rev. C* **73** (2006) 014904
- [34] A. Andronic *et al.*, arXiv:nucl-th/0701079v2 (2007)
- [35] Y. L. Dokshitzer and D. E. Kharzeev, *Phys. Lett. B* **519** (2001) 199
- [36] J. Adams *et al.* (STAR Collaboration), *Phys. Rev. Lett.* **94** (2005) 062301
- [37] S. Eidelman *et al.* (Particle Data Group), *Phys. Lett. B* **592** (2004) 1
- [38] H. Zhang for the STAR Collaboration, *Nucl. Phys. A* **774** (2006) 701
- [39] C. Zhong for the STAR Collaboration, *J. Phys. G* **34** (2007) S741
- [40] X.-N. Wang and M. Gyulassy, *Phys. Rev. D* **44** (1991) 3501-3516
- [41] B. I. Abelev *et al.* (STAR Collaboration), *Phys. Rev. Lett.* **98** (2007) 192301
- [42] A. A. P. Suaide (for the STAR Collaboration), *J. Phys. G* **30** (2004) S1179-S1182
- [43] A. Adare *et al.* (PHENIX Collaboration), *Phys. Rev. Lett.* **97** (2006) 252002
- [44] A. Adare *et al.* (PHENIX Collaboration), *Phys. Rev. Lett.* **98** (2007) 172301
- [45] S. Baumgart for the STAR Collaboration, arXiv:0709.4223v1 [nucl-ex] (2007)
- [46] S. Frixione *et al.*, arXiv:hep-ph/9702287v2 (1997)
- [47] M. Cacciari *et al.*, *Phys. Rev. Lett.* **95** (2005) 122001
- [48] R. Vogt, arXiv:0709.2531v1 [hep-ph] (2007)
- [49] A. A. P. Suaide, *J. Phys. G* **34** (2007) S369
- [50] J. Adams *et al.* (STAR Collaboration), *Phys. Rev. Lett.* **91** (2003) 172302
- [51] M. Djordjevic *et al.*, *Phys. Lett. B* **632** (2006) 81
- [52] N. Armesto *et al.*, *Phys. Lett. B* **637** (2006) 362

- [53] S. Wicks *et al.*, *Nucl. Phys. A* **784** (2007) 426-442
- [54] H. van Hees *et al.*, *Phys. Rev. C* **73** (2006) 034913
- [55] A. Adil and I. Vitev, arXiv:hep-ph/0611109v2 (2006)
- [56] X. Lin (for the STAR collaboration), *J. Phys. G* **34** (2007) S821